Journal of Materials Processing Tech. 297 (2021) 117276

Contents lists available at ScienceDirect

Journal of Materials Processing Tech.

journal homepage: www.elsevier.com/locate/jmatprotec

Evaluation of heat transfer within numerical models of resistance spot welding using high-speed thermography

E. Brizes [a], J. Jaskowiak [a], T. Abke [b], H. Ghassemi-Armaki [c], A.J. Ramirez [a,*]

[a] Department of Materials Science and Engineering, The Ohio State University, 1248 Arthur E. Adams Dr, Columbus, OH, USA
[b] Honda R&D Americas, Inc., 21001 State Route 739, Raymond, OH, 43067, USA
[c] ArcelorMittal Global R&D, 3001 E Columbus Drive, E. Chicago, IN, 46312, USA

ARTICLE INFO

Associate Editor: S.-J. Na

Keywords:
Resistance spot welding
Finite element analysis
High-speed video
Infrared thermal imaging
High-speed thermography
Advanced high-strength steel

ABSTRACT

The automotive industry is demanding more sophisticated resistance spot welding (RSW) models with an emphasis on integrated computational materials engineering (ICME) to better design welded structures. RSW process models are often validated using experimental weld nugget diameter measurements that verify the maximum temperature prediction but not the entire transient temperature response. The accuracy of temperature data on-cooling is essential to reduce error in integrated process-material models during the simulation of microstructural evolution. In this study, two existing 3D finite element (FE) models of RSW (general-purpose and RSW-dedicated) that were previously optimized for 1.5 mm thick Usibor®1500 steel are conventionally validated using experimental nugget diameter and electrode indentation measurements and then modified to represent half-section RSW. The half-section RSW simulation results are directly compared to experimental temperature data captured using high-speed thermography (HST). Analysis of HST showed that the thermal history and $t_{8/5}$ predicted by RSW-dedicated model were more consistent with the HST data, but the general-purpose model more accurately predicted half-section RSW nugget diameter by 8 % and electrode indentation by 11 % as a function of welding current. The models' material properties, specifically workpiece thermal conductivity and specific heat as a function of temperature, had a significant effect on the RSW model temperature fields on-cooling. Overall, HST of half-section RSW provided a quantitative comparison of experimental and simulated temperature results and was a viable technique to validate the thermal history outputted by RSW FE models.

1. Introduction

Resistance spot welding (RSW) is favored in the automotive industry for fast and reliable joining of sheet metal assemblies. Many numerical models of RSW have been developed to optimize process parameters (Nied, 1984) and better understand the underlying mechanisms like residual stresses (Nodeh et al., 2008) and expulsion (Wan et al., 2014). These finite element (FE) models are typically constructed in either 2D axisymmetry or 3D quarter-symmetry with fully- or sequentially-coupled solid-mechanics, heat-transfer, and electric-current analyses (Nielsen et al., 2015b). Because the strength of a spot weld is highly dependent on the size of the weld nugget, FE models are often designed to show agreement between the predicted nugget diameter and experimental nugget diameter data (Eisazadeh et al., 2010). Once validated, the joining process simulation can serve as the foundation of an integrated computational materials engineering (ICME) modeling framework that aims to predict the RSW microstructural and mechanical property gradients (Yang et al., 2006). Such frameworks are in high demand by the automotive industry to enhance the design of welded structures. The accuracy of the temperature data outputted by the FE model is critical for a reliable prediction of the resulting microstructural evolution and to prevent propagation of error within these integrated modeling frameworks.

Currently, the most impactful temperature validation method of RSW modeling is based on comparing simulated to experimental nugget size. This method is used to verify the maximum temperatures predicted by the model, but it is not able to validate the entire transient temperature response. Verification of thermal history on-cooling, specifically the time to cool from 800 °C to 500 °C ($t_{8/5}$), is necessary for accurate microstructural evolution modeling. Thermocouples have been attached

---

[*] Corresponding author at: Department of Materials Science and Engineering, The Ohio State University, 1248 Arthur E. Adams Dr, Columbus, OH, USA.
E-mail address: ramirez.49@osu.edu (A.J. Ramirez).

https://doi.org/10.1016/j.jmatprotec.2021.117276
Received 10 February 2021; Received in revised form 21 June 2021; Accepted 23 June 2021

to the electrode tips (Podržaj and Simonĉiĉ, 2013), sheet-sheet interfaces (Han et al., 1989), and placed inside the molten nugget during RSW to capture temperature data (Alcini, 1990). However, thermocouples introduce many challenges during experimentation such as: the precise machining of a groove to place the thermocouple, current shunting, and thermocouple contact conditions (Eff, 2019). Although not originally developed for simulation validation, high-speed cinematography of half-section RSW has been performed to study nugget growth (Lane et al., 1987) and other phenomena during spot welding such as the effect of workpiece surface coatings (Saha et al., 2015), multi-pulse weld schedules (Kim et al., 2020), and the application of ultrasonic vibration during RSW (Shah and Liu, 2019). Half-section RSW uses machined electrodes and half the process parameters of electrode force and welding current to replicate the current density and joule heating conditions of a standard full-section weld. A schematic of half-section RSW is shown in Fig. 1. To measure the transient temperature response during RSW, Kim and Eagar (1989) were the first to combine high-speed cinematography of half-section RSW with infrared thermography. However, the infrared camera used by Kim et al. was not high-speed (6 frames per second) and the study was limited to the surface of the machined electrodes due to the camera's resolution and temperature range. High-speed thermography technology has advanced, and cameras now have the capability to capture larger temperature ranges at higher framerates using enhanced resolutions.

There are many FE solvers that have RSW simulation capabilities such as *Ansys, Abaqus, Simufact, Sorpas,* and *Sysweld*. In this study, 3D thermo-electro-mechanical models of RSW were constructed in Abaqus CAE and Sorpas 3D. Abaqus CAE is a general-purpose FE modeling suite, while Sorpas 3D is a resistance welding dedicated FE software package. Process- and material-specific properties within the Abaqus and Sorpas simulations were previously optimized by the work of Lu et al. (2018) and internally by Sorpas, respectively. The commercial names of the modeling environments will be replaced with general-purpose (Gen-P) and resistance spot welding dedicated (RSW-D) hereafter. The agreement of the models was first evaluated by comparing simulated to experimental weld nugget diameter and electrode indentation. After the initial agreement with the full-section RSW experimental results was confirmed, the models were then modified to represent the conditions of the half-section RSW process. High-speed cinematography of half-section RSW was used to analyze nugget formation over a range of currents comparable to full-section RSW. From observations and nugget diameter measurements of the high-speed cinematography (HSC), optimized half-section RSW process parameters are determined for high-speed thermography. The transient temperature response from the high-speed thermography (HST) experiments was directly compared to both the Gen-P and RSW-D simulations of half-section RSW. This work aims to determine the viability of HST as a validation method for RSW FE modeling; as well as use HST data to evaluate the FE model parameters and numerical strategies that have the most significant impact on RSW temperature predictions.

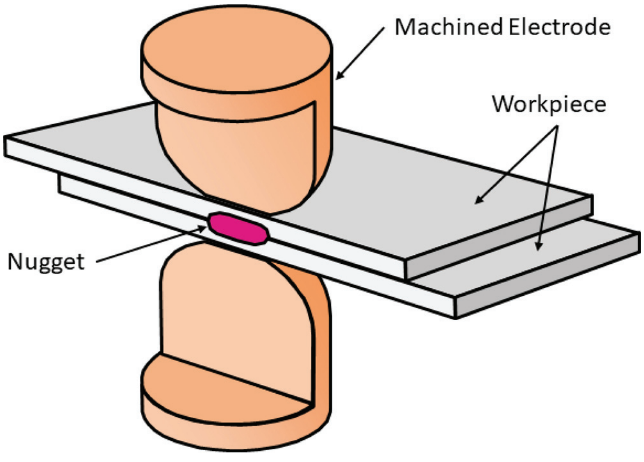

Fig. 1. Schematic of half-section RSW.

2. Approaches

2.1. Numerical modeling of RSW

The development of a RSW process model is labor intensive because it requires expert knowledge of the finite element method and rigorous validation of model inputs such as material properties, part geometries, and contact interactions to achieve meaningful results. To increase simulation reliability and reduce contention of input parameters, existing models that had already been independently optimized were used in this work. Both models under evaluation are shown to successfully simulate the nugget growth during DC spot welding of Usibor®1500 steel, however the models do not implement identical solver strategies or material data.

2.1.1. General-purpose FE model construction

A 3D fully-coupled thermo-electro-mechanical FE model of full-section RSW was constructed to reproduce the work of Lu et al. (2018). The model was designed to simulate the nugget growth during DC spot welding of 1.5 mm thick Usibor®1500 steel using 16 mm dome-type electrodes with a 6 mm diameter face. The Usibor®1500 steel used in both the simulations and experimentation is a second-generation AHSS steel used in hot-forming applications. The chemical composition of the Usibor®1500 steel is shown in Table 1.

Usibor®1500 has an aluminum-silicon (Al-Si) coating that prevents decarburization during hot-stamping and serves as a barrier to oxidation in service. The boundary conditions, load definitions, and material properties of the quarter-symmetric model are consistent with the model of Lu et al., except for the thermal contact conductance at the electrode-sheet and sheet-sheet interfaces. Thermal contact conductance (h_c) was determined using the Mikić elastic correlation (Mikić, 1974):

$$h_c = 1.54 k_h \frac{m}{\sigma}\left(\frac{P\sqrt{2}}{E^{`} m}\right)^{0.94},$$

where k_h is the harmonic mean of the thermal conductivities of the materials in contact, m is the average slope of surface asperities, σ is the standard deviation of the profile heights, and P is the pressure. E' is related to the elastic moduli of the two contacting materials by:

$$E^{`} = (E_1E_2)/\left[E_2(1-v_1^2)+E_1(1-v_2^2)\right],$$

where E is the modulus of elasticity and v is the Poisson's ratio. The effect of the Al-Si coating on the elastic modulus of the Usibor®1500 surface was ignored. The values of m and σ for the Usibor®1500 steel and electrode tip were determined using the profilometry capabilities of an MTS Nanoindenter XP instrumented indenter and verified using optical microscopy of electrode and workpiece cross-sections. The surface parameters used for the electrode and Usibor®1500 steel, alongside the electrode-sheet (E-S) and sheet-sheet (S-S) interfaces are listed in Table 2.

Table 1
Chemical composition of Usibor®1500 steel (maximum wt%) (ArcelorMittal, 2020).

Fe	C	Si	Mn	P	S	Al	B	Ti + Nb	Cr + Mo
Bal.	0.24	0.4	1.4	0.03	0.01	0.01 - 0.1	0.005	0.12	1

Table 2
Surface parameter of the electrode and Usibor®1500 steel for thermal contact conductance of the S-S and E-S interfaces.

Parameter	Electrode	Usibor®1500	E-S Interface	S-S Interface
m	0.45	0.55	0.50	0.55
σ (um)	6.1	16.9	11.5	16.9

2.1.2. RSW-dedicated FE model construction

A similar model of full-section RSW was constructed using the RSW-dedicated FE software. The RSW-D model uses a different numerical coupling strategy in which the mechanical solution is weakly coupled to the thermo-electric solution at each time step. Small time steps are used to maintain solution accuracy despite the weak mechanical coupling (Lövenborn, 2016). A schematic detailing the differences in the numerical coupling strategies between the Gen-P and RSW-D models is shown in Fig. 2. A comprehensive explanation of the RSW-D model's governing equations and finite element formulations is described by Nielsen et al. (2013).

Because the RSW-D environment is intended to be a user-friendly simulation tool, model construction was carried out using predefined 16 mm dome-type electrode and 1.5 mm thick workpiece geometries. The electrical and mechanical boundary conditions were kept default. The default thermal boundary conditions adequately matched the Gen-P model and the experimental conditions. The defined electrical and mechanical loads were consistent with the Gen-P model. Usibor®1500 steel was selected within the RSW-D software's material library, and a 40-micron thick Al-Si coating in the hot-stamped condition was applied to the workpiece surfaces. Thermal contact conductance was modeled using the following equation (Nielsen et al., 2015a):

$$h_c = \frac{1}{\rho_c}, \quad \rho_c = \frac{3\sigma_{soft}}{\sigma_n}\left(\frac{1/k_1 + 1/k_2}{2}\right)$$

where ρ_c is the thermal contact resistance, σ_{soft} is the flow stress of the softer material, σ_n is the normal contact pressure, and k_1 and k_2 are the bulk thermal conductivities of the materials in contact. A comparison of the temperature-dependent specific heat, thermal conductivity, and electrical resistivity of Usibor®1500 steel, and the temperature-pressure-dependent thermal contact conductance of the electrode-sheet interface in the Gen-P and RSW-D simulations is shown in Fig. 3. Note that the RSW-D software's coating and workpiece material property data are proprietary, and any material data shown for the RSW-D simulations comes from previously published data (Lövenborn, 2016).

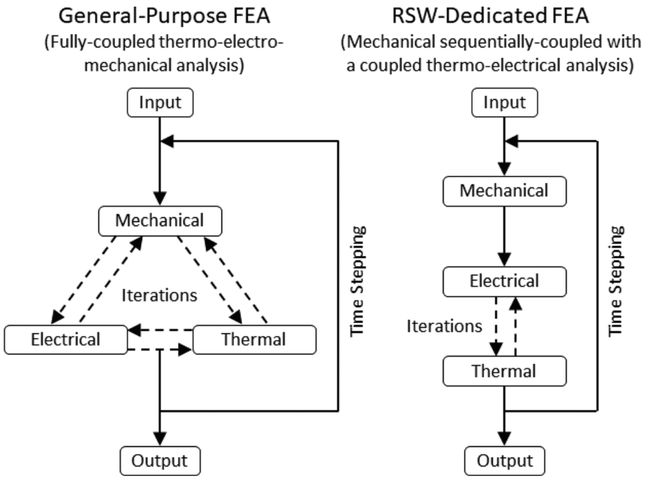

Fig. 2. Differences in the numerical coupling of the thermal, electrical, and mechanical solutions within the Gen-P and RSW-D models.

2.2. Adaptation of numerical models for half-section RSW

The boundary conditions of the full-section models were not representative of the half-section RSW process. To adapt the full-section model to simulate half-section RSW the following changes were made.

Within the Gen-P model, the symmetry along the YZ-plane was removed. A convective heat loss due to ambient air was placed on the surfaces of the YZ-plane using a film coefficient of $19.4\ \mathrm{W}/(\mathrm{m}^2\mathrm{K})$. The displacements of the regions of the Usibor®1500 sheets on the YZ-plane that were beyond the mesh created to capture the heat-affected zone (HAZ) were constrained in the X and Z directions to represent the fixturing used during experimentation. A schematic that compares the boundary conditions of the full- and half-section Gen-P FE model is shown in Fig. 4.

For the RSW-D model, once the YZ-plane symmetry was deselected the same convective heat loss from ambient air that was applied to the workpiece surfaces was automatically applied to the YZ-plane surface. Unlike the Gen-P model, no regions of the YZ-plane were fixed in the X and Z directions.

2.3. RSW experimentation for full-section FE model validation

Two sheets of the 1.5 mm thick Usibor®1500 steel were welded in a lap-joint configuration using a pedestal-type Mid-Frequency Direct Current (MFDC) resistance spot welder. The single-pulse weld schedule used in the full-section RSW experimentation and modified for the half-section RSW experiments was based on Table 58 of the AWS C1.1M standard (American Welding Society, 2019). Welds were made at currents ranging from 4.5 kA to 8.5 kA in increments of 0.5kA using a constant weld time of 333 ms, and at weld times ranging from 0 ms to 333 ms in increments of 33 ms at a constant current of 6.25kA. The process parameters for the current range and time range experiments of the full-section welds are listed in Table 3. The extended squeeze and hold times are not representative of weld schedules used in industry but were necessary to stabilize the position of the joint during high-speed video capture of the half-section RSW. For consistency, the full-section experiments also used the extended squeeze and hold times.

The welds were then cross-sectioned at the centerline, ground from 240-grit to 1200-grit using silicon-carbide paper and etched using a 2 % Nital solution to reveal the weld nugget and HAZ microstructure. Optical microscopy was used to image the weld cross-sections. Measurements of the weld nugget diameter and joint thickness were taken from the images using ImageJ, an open-source image processing program. A combined photomicrograph and depiction of the maximum temperatures predicted by the simulation with the locations of the measurements and relevant HAZs is shown in Fig. 5. The joint thickness measurements were used to calculate electrode indentation per the AWS D8.1 M standard (American Welding Society, 2005). Electrode indentation was used as an additional metric of comparison because it is critical to the load carrying capacity of the joint.

2.4. High-speed cinematography of half-section RSW

Half-section welds were performed by aligning two sheets of Usibor®1500 steel with the machined electrodes. A fixture was fabricated to maintain consistent placement of the sheets across all experiments. The sheared edges of the steel were ground with 240-grit silicon-carbide paper to create a flat surface without excessive reflectivity. The electrode force and welding current were reduced to half the values used in the full-section experiments to maintain heat generation conditions comparable to the full-section welds (Cho and Rhee, 2003). Welds were made at currents ranging from 2.25 kA to 4.25 kA in increments of 0.25kA using a constant weld time of 333 ms. The process parameters for the half-section cinematography welds are listed in Table 4.

A Photron FASTCAM SA-X2 camera fitted with a Nikon AF-S VR Micro-Nikkor 105 mm f/2.8 G macro lens was used for high-speed

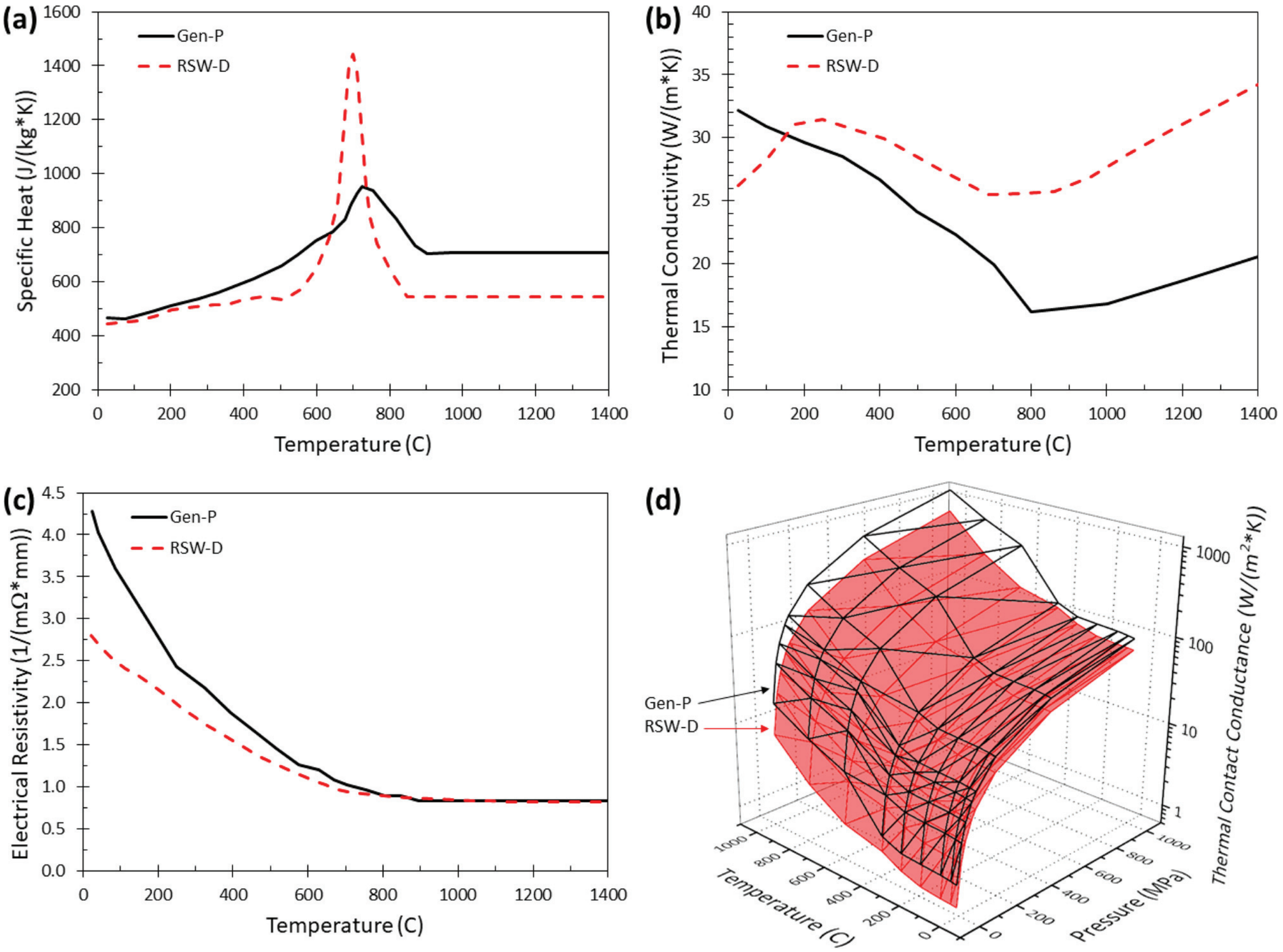

Fig. 3. Comparison of the temperature-dependent (a) specific heat, (b) thermal conductivity, and (c) electrical resistivity of Usibor®1500 steel, and temperature-pressure-dependent (d) thermal contact conductance of the electrode-sheet interface in the Gen-P and RSW-D simulations.

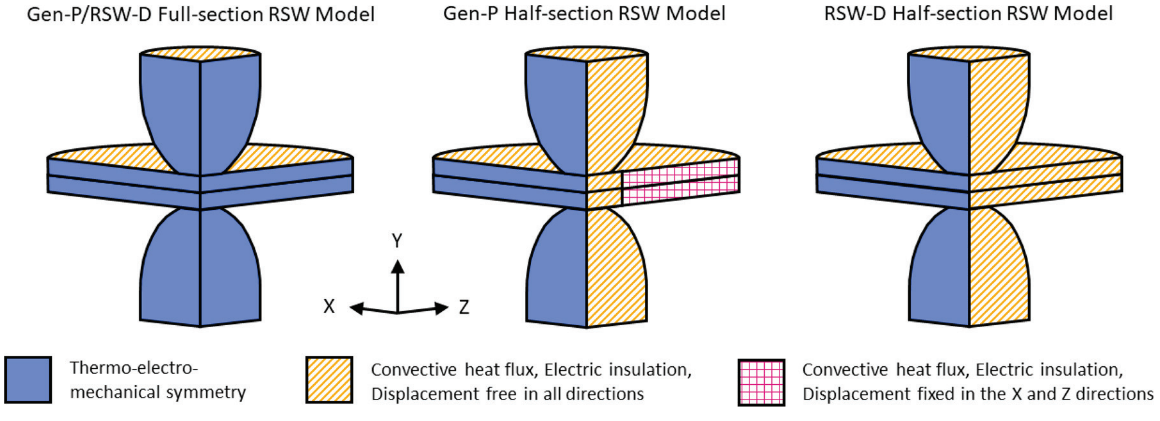

Fig. 4. Schematic of boundary conditions for the full-section (left) and half-section RSW Gen-P (middle) and RSW-D (right) FE models.

Table 3
Full-section RSW parameters for 1.5 mm thick Usibor®1500 steel in a two-sheet lap joint configuration.

Variable Parameter	Electrode Force (kgf)	Squeeze Time (ms)	Weld Current (kA)	Weld Time (ms)	Hold Time (ms)
Weld Current	450	500	4.5–8.5	333	1000
Weld Time	450	500	6.25	0–333	1000

cinematography. A #47 blue filter was placed on the lens to reduce overexposure of the weld nugget. The camera was positioned normal to the vertical plane of the half-section RSW and had a working distance of 32 cm. Video was captured in 12-bit monochrome at 1000 frames per second with a resolution of 1024 pixels x 1024 pixels. Still images of the high-speed video were taken in increments of 33 frames (33 ms) from the start of the welding portion of the weld schedule. Measurements of the weld nugget diameter and joint thickness were taken from the images using ImageJ. A still image with the locations of the measurements is shown in Fig. 6.

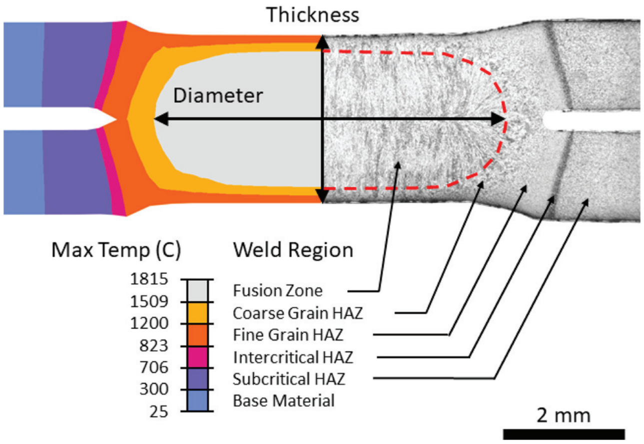

Fig. 5. Measurements of nugget diameter and joint thickness on a spot weld cross-section. (For interpretation of the references to colour in this figure text, the reader is referred to the web version of this article.)

Table 4
Half-section RSW parameters for 1.5 mm thick Usibor®1500 steel in a two-sheet lap joint configuration.

Capture Method	Electrode Force (kgf)	Squeeze Time (ms)	Weld Current (kA)	Weld Time (ms)	Hold Time (ms)
Cinematography	225	500	2.25−4.25	333	1000
Thermography	225	500	3.5	333	1000

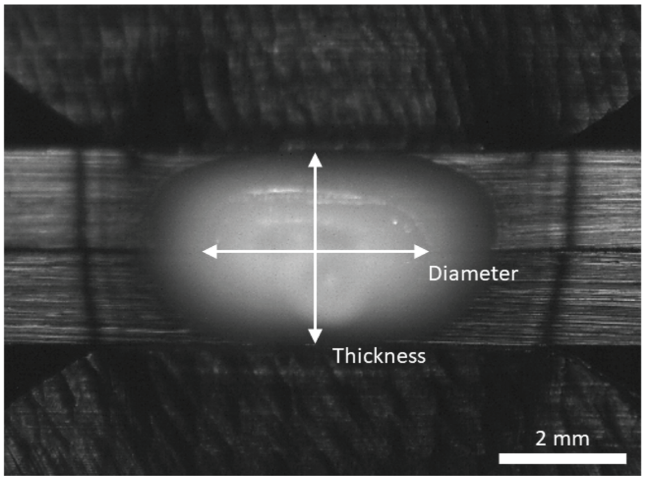

Fig. 6. Measurements of nugget diameter and joint thickness on a still image from high-speed cinematography.

2.5. *High-speed thermography of half-section RSW*

The experimental setup for high-speed thermography was identical to the high-speed cinematography setup. The data and observations from high-speed cinematography were used to determine the optimal welding current of 3.5 kA to achieve a nugget with a diameter greater than the minimum diameter specified by industry and minimal extrusion of the molten metal to prevent obstruction of view of the sheet surface. The welding current of 3.5kA was also selected because it created a nugget with a diameter comparable to the time range performed during the full-section RSW experimentation. A more detailed explanation of the parameter optimization is provided in Section 3.3. The process parameters for the half-section thermography welds are listed in Table 4.

High-speed thermography was conducted using a FLIR A6750 sc infrared camera equipped with a 50 mm lens and an ND2 filter to measure temperatures ranging from 250 °C to 2000 °C. The camera was positioned normal to the vertical plane of the half-section RSW and had a working distance of 50 cm. The recording was performed at 406 frames per second with a resolution of 320 pixels x 256 pixels. The emissivity value of 0.6 was calibrated for a ground steel surface between 400 °C–900 °C for a more accurate reading of temperatures in the $t_{8/5}$ range (Bramson, 1968). Note the emissivity of steel changes as a function of temperature and surface conditions, however a single value was used in processing of the thermal camera data due to software limitations.

3. Results and discussion

3.1. *Validation of full-section RSW FE models*

The validity of a FE model is judged by its ability to consistently reproduce experimental results over a wide range of process parameters. To determine if the Gen-P and RSW-D models are valid, measurements of nugget diameter and electrode indentation are compared over a range of applied welding currents at a single weld time and over a range of time at a single weld current. As previously mentioned, nugget diameter and electrode indentation are critical metrics of comparison because they determine the load carrying capacity of the joint.

Fig. 7(a) and (b) depict the full-section RSW nugget diameter and electrode indentation measurements from the current range experiments plotted with the Gen-P and RSW-D simulation results. Fig. 7(a) shows that the nugget diameters predicted by both the Gen-P and RSW-D models are consistent with the experimentally measured nugget diameters across the entire current range. The 0 mm value of the RSW-D model at a welding current of 4.5kA illustrates how sharply nugget diameters increase once the minimum current to achieve a nugget is applied. Agreement between the simulated and experimental nugget diameters is expected because nugget diameter data is often used to optimize RSW models. The electrode indentation measurements from the full-section current range experiment are plotted with the simulation data in Fig. 7(b). On average, the Gen-P model underpredicted the amount of electrode indentation by 12 %, and the RSW-D model underpredicted the electrode indentation by 37 %. Although both models underpredicted the electrode indentation, the upward trend or indentation increase as a function of current was consistent with the experiments.

The time range experimentation, in which measurements were taken from a single welding current of 6.25kA in intervals of 33 ms, is shown compared to the model results in Fig. 7(c) and (d). Fig. 7(c) demonstrates that even though the current range nugget diameter measurements agreed with the experimental data, the nugget growth as a function of time can deviate from the experimental results. The Gen-P model had better agreement with the experimental data than the RSW-D model. The RSW-D simulation underpredicted the nugget diameter from 0 ms to 233 ms then overpredicted the final diameter at 333 ms by 30 %. This differing trend is attributed to the differences in Usibor®1500 thermal properties inputted into the models. Fig. 3(b) shows that the RSW-D model has a higher thermal conductivity at higher temperatures, which removes heat faster through conduction within the workpiece and ultimately reduces the amount of heat buildup at the sheet-sheet interface. Both models use values of thermal conductivity within the expected range of steels, however the Gen-P model's thermal conductivity approaches a minimum nearing 15 W/(m*K) at 800 °C. A faster buildup of heat at the sheet-sheet interface increases the rate of weld nugget formation. The electrode indentation data from the time range experiments is shown in Fig. 7(d). Like the current range data, electrode indentation was underpredicted by both models with an average error of 20 % and 44 % for the Gen-P and RSW-D models, respectively. However, once the indentation started, the rate of indentation was consistent at 0.15 mm/s for all three datasets. Because the

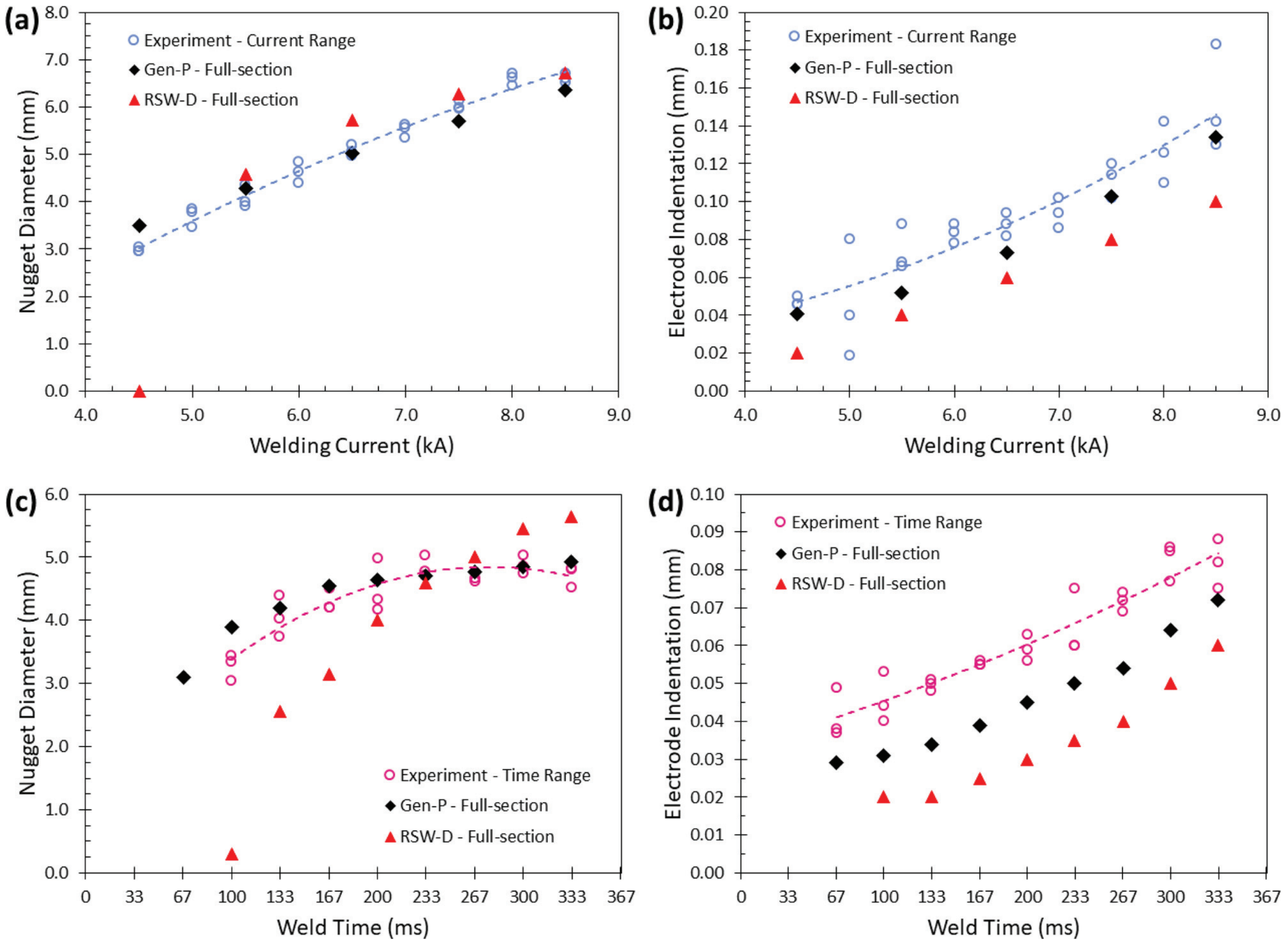

Fig. 7. Comparison of (a, c) nugget diameter and (b, d) electrode indentation measurements from the full-section RSW (a, b) current range and (c, d) time range experimentation to the full-section RSW Gen-P and RSW-D simulations.

RSW-D model uses a numerical coupling strategy in which the mechanical solution is weakly coupled to the thermo-electric solution, it is likely that a lagging mechanical solution combined with a shorter period of time at high temperatures (higher thermal conductivity) resulting in a larger error in the prediction of electrode indentation.

The agreement between the simulated and experimental nugget diameter measurements in conjunction with the matching trends of electrode indentation as a function of weld time and current supports the validity of the Gen-P and RSW-D models. Valid full-section models increase the reliability of the results when the models are modified to represent half-section RSW.

3.2. Comparison of high-speed cinematography and half-section RSW FE models

The Gen-P and RSW-D models were modified to simulate half-section RSW, as described in Section 2.2. To determine if the simulations were consistent with the half-section experimental conditions, nugget diameter and electrode indentation measurements taken from still images of the HSC were compared to measurements from the half-section simulations. A visual representation of the HSC images compared to the temperature field of the Gen-P model can be seen in Fig. 8. Note the darkening of the HAZ in the HSC images and the positional similarity to the HAZ temperature regions in the Gen-P model.

Fig. 9(a) shows the nugget diameter as a function of welding current predicted by the Gen-P model is consistent with HSC experimental data having values within 0.5 mm or an average error of 5 %. The RSW-D model also shows good agreement but slightly underpredicts the nugget diameter by an average error of 13 % or a difference of 0.7 mm. Neither the Gen-P nor RSW-D results display agreement with the experimental electrode indentation vs. welding current data shown in Fig. 9(b). The Gen-P electrode indentation better follows the trend but overpredicts the experimental results by an average of 18 %. The RSW-D electrode indentation as a function of welding current significantly underpredicts the experimental values by 53 % at the lower end of the current range but becomes more consistent as the applied current approaches the maximum of 4.0kA to achieve an average error of 29 %.

Both the Gen-P and RSW-D models agree with the trend and magnitude of the half-section experiment nugget diameter measurements as a function of time shown in Fig. 9(c). A significant deviation of the half-section Gen-P and RSW-D time range data from the experimental measurements of electrode indentation can be seen in Fig. 9(d). Although initially following the experimental trend until 233 ms, the Gen-P eventually overpredicted the final electrode indentation at 333 ms by 0.024 mm or 19 %. The RSW-D model consistently underpredicted electrode indentation by 0.033 mm, but the trend or rate of indentation agreed better with the experimental results than the Gen-P model.

Overall, a comparison of both the full-section results in Fig. 7 and the half-section results in Fig. 9 shows that neither model significantly outperformed the other in their abilities to predict nugget diameter and electrode indentation. In many cases, the Gen-P model exhibited a smaller error, but both models were able to successfully predict nugget diameters over a range of currents in both the full- and half-section configurations. As previously stated, the issue with basing the success of the model solely on the nugget diameter and electrode indentation is that only the on-heating portion of the weld cycle is evaluated. For a

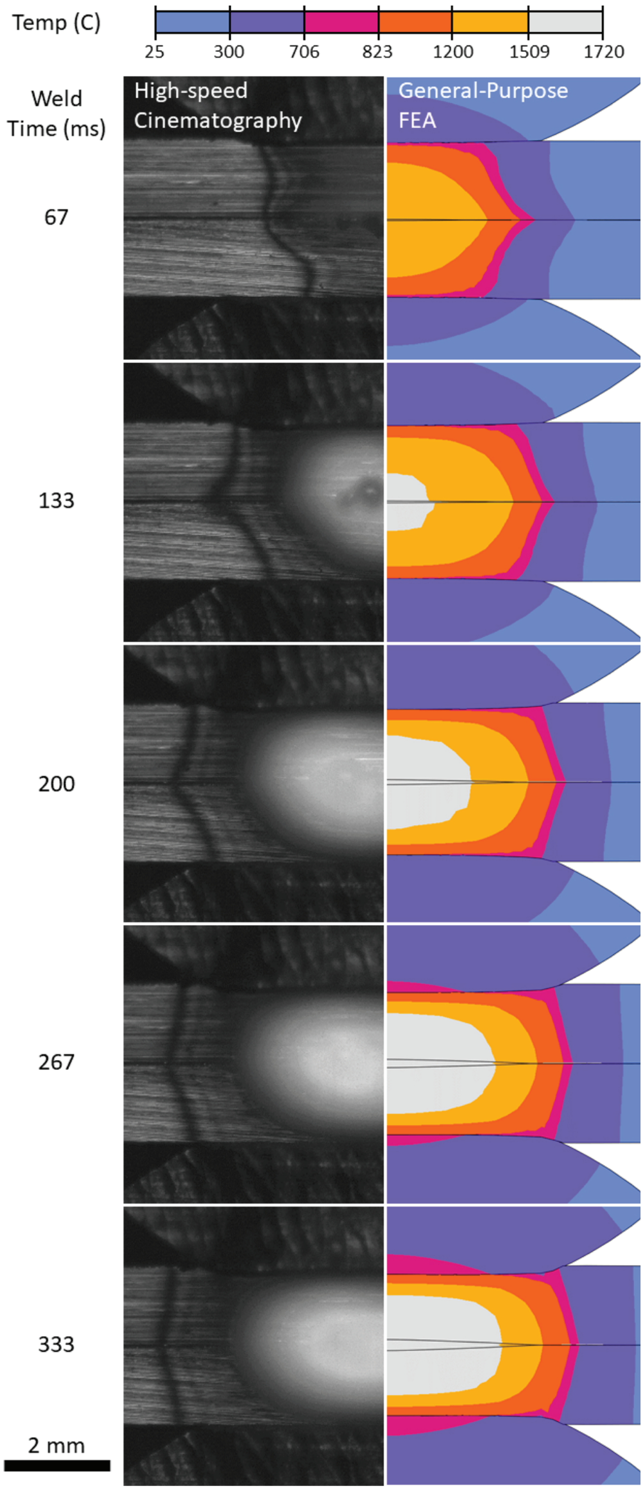

Fig. 8. Comparison of images from HSC (left) to the temperature field of the Gen-P simulation (right) in time intervals of 67 ms.

complete analysis of the temperature response, on-cooling data must also be compared. The use of HST is intended to make the on-cooling comparison simpler and achieve a higher degree of fidelity. In the next sections, the optimization of the process parameters and results of the HST will be discussed for a better understanding of each FE model's ability to predict temperatures on-cooling.

3.3. Optimization of half-section RSW process parameters for high-speed thermography

In addition to providing a comparison between experimental and simulated half-section RSW, the nugget diameter data and observations from HSC were used to optimize the half-section process parameters for HST. Fig. 10 graphically illustrates the rationale supporting the determination of HST process parameters. The half-section RSW nugget diameters from the current range analysis are plotted alongside the full-section RSW data with the welding currents proportional to heat input. The horizontal line marks the minimum nugget diameter determined by the AWS C1.1 M standard of $4\sqrt{\bar{t}}$, where $\bar{t}$ is the average thickness of the sheets to be welded (American Welding Society, 2019). Any nugget diameter below the horizontal line readily fails strength requirements and is deemed inadequate. Because it is important to use HST to capture the temperature response of the nugget sizes comparable to welds performed in industry, the half-section welding current for HST needed to be at or above 3.5kA. Also, a larger nugget creates a larger temperature field that can be captured by the HST camera. Observationally, higher half-section welding currents created more extrusion of the molten weld material. The top-right image within Fig. 10 shows the extent of the molten material and how it extends far beyond the vertical plane. Excessive extrusion of the molten weld material limited the HST camera's visibility of the entire nugget and HAZ regions at welding currents above 3.75kA. For this reason, an optimal half-section welding current lies to the left of the vertical line shown in Fig. 10. The optimized half-section welding current for HST was selected to be 3.5kA. From the plot in Fig. 10, it can be seen that a half-section weld using 3.5kA creates a nugget diameter of 4.9 mm which corresponds to the same nugget size as a full-section RSW conducted at 6.25kA.

3.4. Comparison of high-speed thermography and half-section RSW FE models

The experimental temperature field captured by the HST camera allows for a direct comparison to the temperature vs. position data outputted by the FE models. The progression of the half-section RSW surface temperature during the welding portion of the process, also called on-heating, is shown in Fig. 11. As stated in Section 2.5, the HST camera was able to capture data within a temperature range of 250 °C–2000 °C, but the emissivity was calibrated to read temperatures between 400 °C–900 °C on a ground surface. HST regions above 900 °C are analyzed with caution. Additionally, the surface characteristic of any regions that transformed into liquid (temperatures above 1509 °C) changed from ground to smooth and are expected to vary from the calibrated emissivity.

From visual interpretation of the temperature distribution images in Fig. 11, the RSW-D model has a higher degree of similarity to the HST images, especially at the 67 ms and 133 ms weld times. The Gen-P model exhibits a region of molten weld metal where temperatures exceed 1509 °C at the weld time of 133 ms while both the HST and RSW-D images show first evidence of nugget formation at the 200 ms image. This result is consistent with the data in Fig. 9(c) where the experimental nugget diameter is slightly overpredicted by the Gen-P model at a time of 133 ms. The SCHAZ, ICHAZ, and FGHAZ regions depicted first in Fig. 5 and shown as the dark blue, magenta, and orange regions of the images, respectively, are most accurate as their magnitudes are within the calibrated temperature range. With these regions as the focus of comparison, the experimental HST image at 66 ms more closely resembles the RSW-D simulation. However, there is not a significant difference between the position of SCHAZ, ICHAZ, and FGHAZ within the HST, Gen-P, and RSW-D images at 133 ms–333 ms. Such an interpretation shows that both FE models adequately generated an accurate peak temperature field at the end of the welding cycle (333 ms).

The on-cooling temperature field images of the half-section

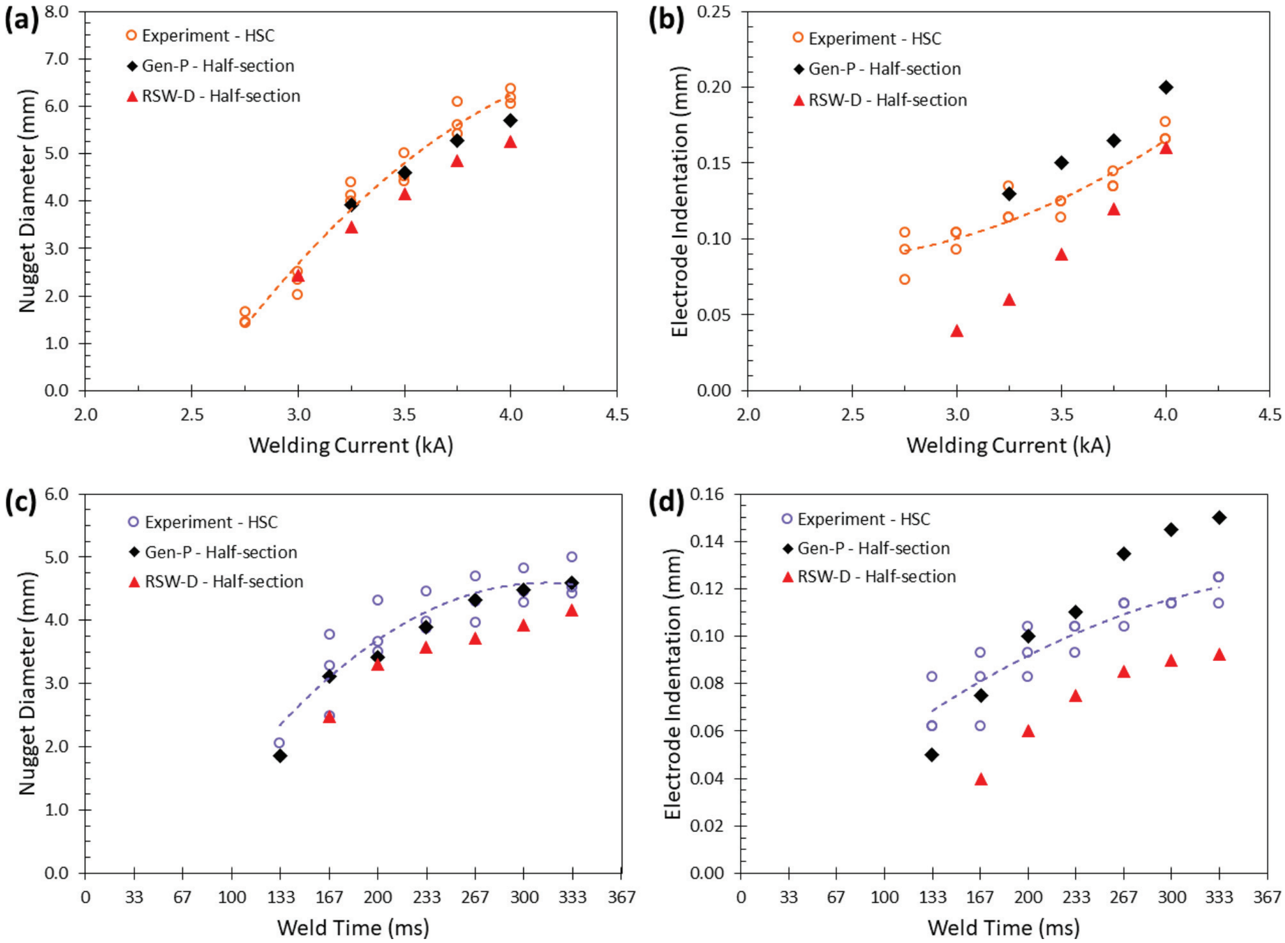

Fig. 9. Comparison of (a, c) nugget diameter and (b, d) electrode indentation measurements from the half-section RSW (a, b) current range and (c, d) time range experimentation to the half-section RSW Gen-P and RSW-D simulations.

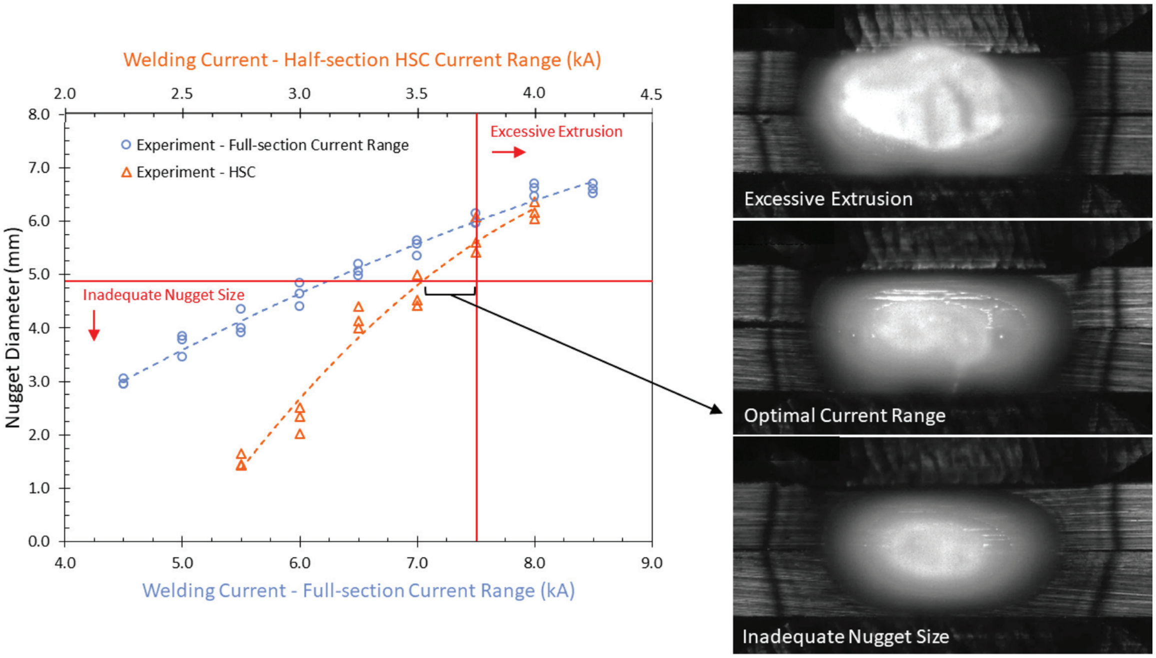

Fig. 10. High-speed thermography welding current optimization using a combined full- and half-section experimental nugget diameter plot (left) and images of weld metal extrusion during half-section RSW (right).

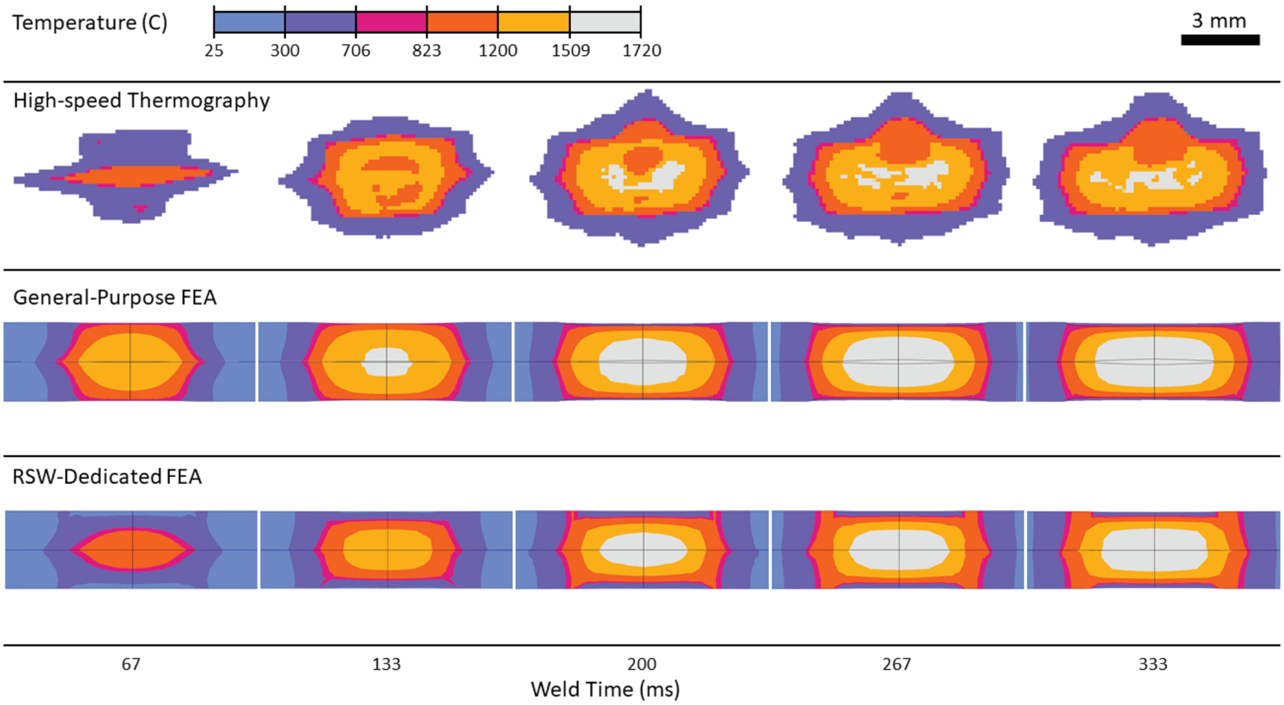

Fig. 11. Comparison of the HST (top), Gen-P model (middle), and RSW-D model (bottom) on-heating temperature fields as a function of time in intervals of 67 ms.

experimentation and simulations are shown in Fig. 12. The images were taken from the beginning of the hold portion of the weld schedule in time intervals of 100 ms. At first the position of the ICHAZ and FGHAZ regions of the Gen-P image at 100 ms were consistent with the HST regions, but as the hold time extended to 500 ms the Gen-P surface temperatures above 823 °C persisted longer and covered a larger area then the HST. In contrast, the higher temperature regions of the RSW-D simulation such as the FGHAZ and ICHAZ have disappeared from the temperature field images by the hold time of 300 ms. The slower cooling of the Gen-P model is attributed to the lower thermal conductivity and higher specific heat of Usibor®1500 steel used in the Gen-P simulation. The low Usibor®1500 thermal conductivity is the primary factor because the electrode-sheet thermal contact conductance used in the Gen-P model is higher across all temperatures and contact pressures than the RSW-D model shown in Fig. 3(c). In theory, a higher thermal contact conductance is expected to allow the electrodes in the Gen-P model to conduct heat away from the nugget faster than the RSW-D model, but the Usibor®1500 thermal conductivity is restricting the conduction of heat. On the contrary, the RSW-D images at hold times of 300 ms and 400 ms show the light blue regions where temperatures are

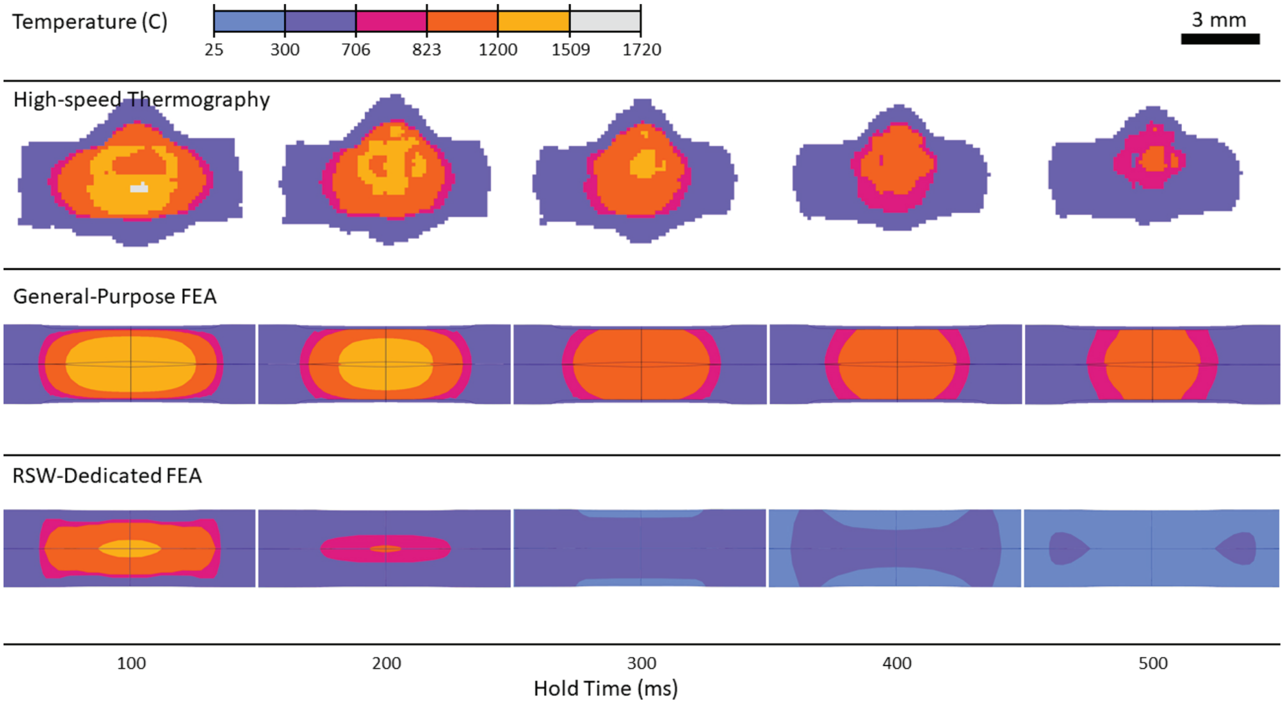

Fig. 12. Comparison of the HST (top), Gen-P model (middle), and RSW-D model (bottom) on-cooling temperature fields as a function of time in intervals of 100 ms.

under 300 °C initiate at the electrode-sheet interface. This observation points to the electrodes acting as a greater heat sink in the RSW-D simulation.

The thermal histories of the HST experimentation and simulations are compared in Fig. 13. The X and Y positions of the points from which the thermal history data was extracted were consistent across all three datasets. The on-heating portion of the thermal history curves from 0 ms to 0.333 s reinforces the agreement stated earlier based on the nugget diameter measurements and temperature field analysis. The temperatures of the Gen-P model seen in Fig. 13(a) are higher than the HST data immediately after peak temperature is reached at 0.333 s and remain higher by around 200 °C until the last plotted temperature at 1.0 s. Comparing the thermal history of the RSW-D model to the HST data in Fig. 13(b), the cooling rates are consistent from 0.333 s–0.6 s and then the temperatures of the CGHAZ, FGHAZ, and ICHAZ drop below the experimental HST data after 0.6 s–0.7 s.

As previously stated, an accurate prediction of time to cool from 800 °C to 500 °C ($t_{8/5}$) is necessary for steel microstructural evolution modeling. Within this temperature range, important microstructural changes occur that can alter the final mechanical properties and ultimately the strength of the welded joint. The $t_{8/5}$ was determined for the HST data and the external surface of the Gen-P and RSW-D simulations. The time values are graphed as a function of position in contour plots shown in Fig. 14. The light blue end of the time spectrum where the $t_{8/5}$ approaches 0 s corresponds to a faster cooling rate while the orange end of the spectrum where the $t_{8/5}$ approaches 1 s corresponds to slower cooling rates. Based on the color gradients of all three plots, the HST $t_{8/5}$ as a function of position is more consistent with the RSW-D model than the Gen-P model. The $t_{8/5}$ in the SCHAZ region of the HST and RSW-D plots are near 0.2 s–0.3 s, while the same region in the Gen-P plot reaches 0.5 s–0.6 s. From visual inspection of Fig. 14, the magenta hue that dominates the Gen-P plot overpredicts the $t_{8/5}$ by a factor of 2 in comparison to the HST and RSW-D plots. The higher $t_{8/5}$ values in the central region of the HST plot can be attributed to the extrusion of the molten weld nugget that is less prominent in the FE simulations. As the molten material extends beyond the vertical plane, it experiences a reduced amount of cooling and heat conduction from the bulk Usibor®1500 material. Note that both models predicted the experimentally confirmed trend of an increased $t_{8/5}$ near the outer edges of electrode-sheet interfaces. These regions experience a high amount of heat generation due to its proximity to the electrode-sheet interface and have lesser cooling from the electrode as the pressure from the electrode force diminishes further from the vertical centerline.

3.5. On the viability of HST as a RSW FE model validation technique

HST was able to consistently and effectively record the thermal history of half-section RSW. From the thermal images, a visual comparison of the half-section experiments and simulations is easily performed. More importantly, the quantitative measurements of temperature as a function of position allow for a direct numerical comparison of the experimental and simulated results. The HST data could also be used to calibrate FE models of RSW. For example, now that the Gen-P model is known to cool slower than the HST data and RSW-D model, the Gen-P model parameters and boundary conditions can be altered to produce more accurate results. Ideally, material properties should not be manipulated to create better FE model results. However, the Usibor®1500 thermal conductivity used in the Gen-P simulation can be increased to remove heat from the weld nugget and HAZ regions faster.

HST outperforms other temperature collection methods like thermocouples in terms of volume of data, but the reliability of the measurement is highly dependent on the emissivity value programmed into the data analysis software. Emissivity values for materials with various surface preparations can be readily looked up in literature, but the direct measurement of emissivity of a specific material surface is more involved. Depending on the required precision or if the emissivity of the material varies greatly as a function of temperature, HST may not be an ideal temperature measurement technique. As stated in Section 2.5, the emissivity value was set at 0.6 to best record temperatures of a ground steel surface within a range of 400 °C–900 °C.

The success of the HST on half-section RSW is also dependent on the camera's ability to view the workpiece surfaces. As shown in Fig. 10, excessive extrusion of the molten weld material can obstruct the

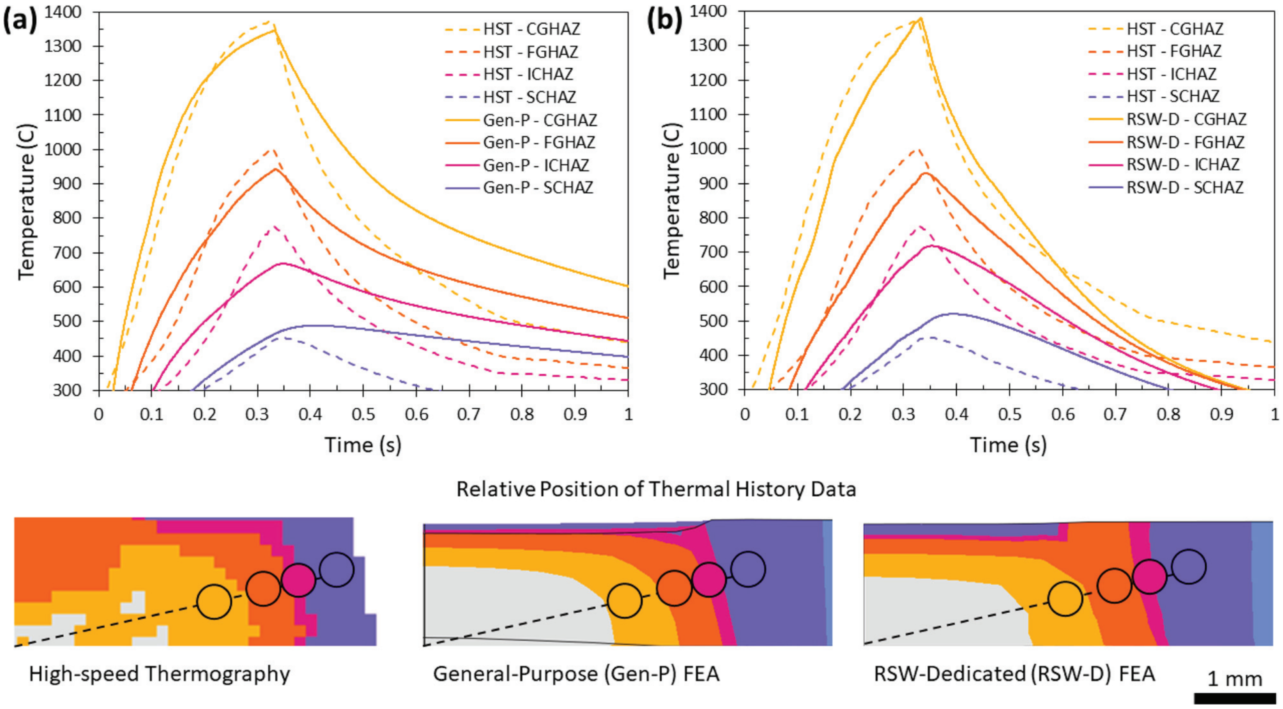

Fig. 13. Thermal history plots comparing the HST data toto the Gen-P model (left) and the RSW-D model (right).

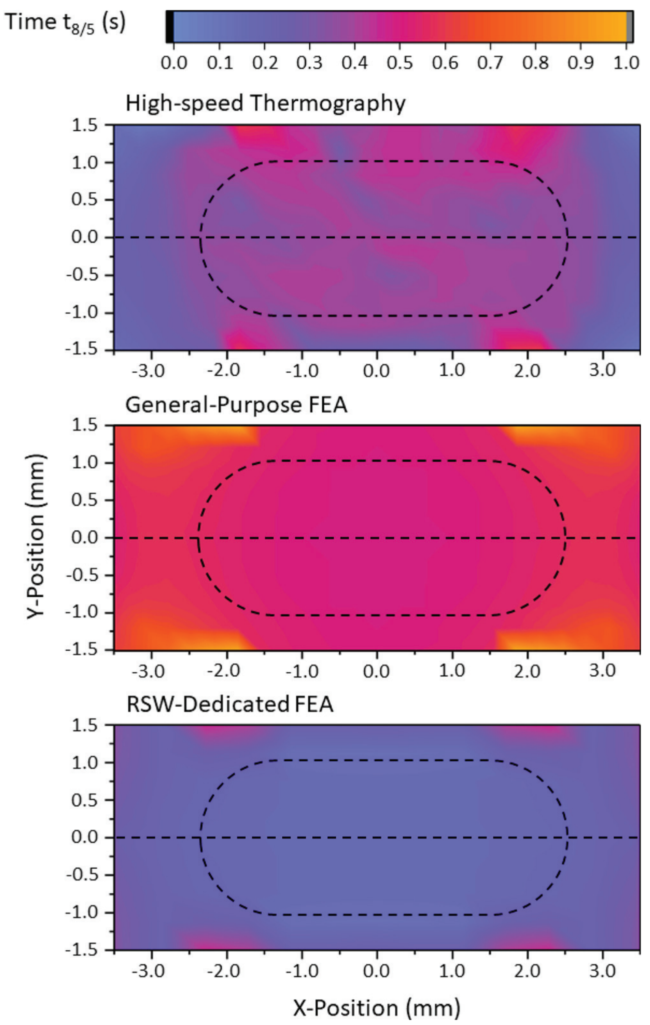

Fig. 14. Contour plots of the $t_{8/5}$ for the HST (top), Gen-P model (middle), and RSW-D model (bottom). (For interpretation of the references to colour in this figure text, the reader is referred to the web version of this article.)

camera's view of the HAZs and reduce the amount of usable temperature data. The amount of material extrusion corresponds with the weld schedule used during half-section RSW. Higher values of applied welding current are more likely to produce a large volume of molten material that will be squeezed out at the sheet-sheet interface. Additionally, the single-pulse weld schedule used in this work is simpler than the multi-pulse schedules used in industry. Weld schedules with multiple pulses are not directly comparable between half- and full-section RSW because as soon as the molten material begins to extrude from the workpiece surface, the physical similarity of half- to full-section RSW decreases.

The temperature data collected through HST was critical in the analysis of the cooling rates predicted by the Gen-P and RSW-D models. Based on the comparison in this work, the RSW-D model had better agreement with the experimental HST and would be more useful when accurate thermal predictions are needed. This is important because without the temperature measurements on-cooling, users of the FE models are unaware of the accuracy of the predictions. If RSW models with a large degree of error on-cooling are used in integrated modeling frameworks to predict microstructural evolution, the resulting microstructural prediction will be incorrect. More importantly, microstructural models calibrated using inaccurate FE model cooling rates will have decreased fidelity and limited applicability. HST of half-section RSW provides a quantitative means of assessment to prevent such a mistake from occurring.

4. Conclusions

In summary, two 3D FE models of full-section RSW were validated using nugget diameter and electrode indentation measurements and then modified to represent half-section RSW. HSC was used to quantify the weld nugget growth and electrode indentation of half-section RSW and optimize the welding current for HST. HST was conducted on the half-section RSW and used to compare the thermal histories predicted by the models to experimental results and assess the viability of HST as a RSW model validation technique. From the detailed comparison, the following conclusions can be drawn:

1 High-speed thermography is a viable method of validating half-section RSW thermal history. Recording using a FLIR A6750 sc infrared camera equipped with a 50 mm lens and an ND2 filter at 406 frames per second with a resolution of 320 pixels x 256 pixels was sufficient to capture the desired temperatures ranging from 250 °C to 2000 °C at an appropriate timescale. The measurement technique excels at generating temperature fields that can be directly compared to simulation results. However, care must be taken when determining an appropriate value of surface emissivity. Also, half-section weld schedules need to be optimized to limit the amount of extrusion during weld nugget growth, which can obstruct the camera's view of the HAZ. In addition to validation, it is predicted that HST can also be used to optimize parameters within half-section and full-section RSW models to better fit experimental results of temperature on-cooling.

2 The overall thermal history and $t_{8/5}$ predicted by RSW-D model are more consistent with the HST data than the Gen-P model. The SCHAZ $t_{8/5}$ measured by HST and outputted by the RSW-D model were between 0.2 s–0.3 s, while the Gen-P model overpredicted the $t_{8/5}$ in this area by a factor of 2 with values nearing 0.6 s. Both models adequately predicted the peak temperature field and temperature on-heating, however the temperature on-cooling outputted by the RSW-D model would better predict microstructural evolution in an integrated modeling framework. The Gen-P model exhibited greater fidelity when predicting the nugget diameter and electrode indentation as a function of time and welding current for both the full- and half-section RSW experimentation. Any arguments made comparing the efficacy or value of each model, specifically regarding the simulation software, would be futile.

3 Accurate prediction of RSW temperature fields on-cooling is highly dependent on workpiece thermal properties. Beware of using RSW models calibrated using only nugget diameter data. This is because RSW FE model users may be tempted to adjust workpiece thermal conductivity or specific heat to increase the heat buildup and overall temperature magnitude at the sheet-sheet interface for better predictions of nugget diameter and electrode indentation. Although a lower workpiece thermal conductivity created better agreement on nugget formation, it reduced the accuracy of the model's on-cooling temperature output.

CRediT authorship contribution statement

E. Brizes: Methodology, Software, Formal analysis, Writing - original draft. **J. Jaskowiak:** Investigation, Data curation. **T. Abke:** Supervision, Conceptualization. **H. Ghassemi-Armaki:** Resources, Writing - review & editing. **A.J. Ramirez:** Project administration, Funding acquisition.

Declaration of Competing Interest

The authors declare that they have no known competing financial interests or personal relationships that could have appeared to influence the work reported in this paper.

Acknowledgments

This work had support from Honda R&D Americas, Inc. and ArcelorMittal Global R&D. Experimentation was assisted by The Ohio State University graduate research associate Bryan Lara, undergraduate researcher River Carpenter, and the welding engineering capstone group members: Christopher Dugan and Drew Hickman. Special thanks to Jonathan Hendrix of the Metro High School in Columbus, OH for the design and 3D-printing of the fixture used during half-section RSW. The authors would like to acknowledge the Manufacturing and Materials Joining Innovation Center (Ma2JIC), made possible through an award (1822144) from the National Science Foundation Industry University Cooperative Research Center program (IUCRC), for financial and infrastructural support. The authors also thank Luvata Ohio, Inc. for providing the electrodes and ArcelorMittal Global R&D for providing the Usibor®1500 steel used during RSW experimentation.

Appendix A. Supplementary video

A supplementary video related to this article can be found, in the online version, at doi:https://doi.org/10.1016/j.jmatprotec.2021.117276.

References

Alcini, W.V., 1990. Experimental measurement of liquid nugget heat convection in spot welding. Weld. J. 69, 177–180.

American Welding Society, 2005. D8.7M Recommended Practices for Automotive Weld Quality- Resistance Spot Welding, 2nd ed. Miami, FL.

American Welding Society, 2019. AWS C1.1M/C1.1 Recommended Practices for Resistance Welding, 6th ed. Miami, FL.

ArcelorMittal, 2020. Steels for Hot Stamping - Usibor and Ductibor [WWW Document]. Press Hardenable Steels. URL https://automotive.arcelormittal.com/products/flat/PHS/usibor_ductibor (accessed 6.28.20).

Bramson, M.A., 1968. Infrared Radiation: A Handbook for Applications, Optical Physics and Engineering. Springer US, Boston, MA. https://doi.org/10.1007/978-2-8178-0363-0_8.

Cho, Y., Rhee, S., 2003. Experimental study of nugget formation in resistance spot welding. Weld. J. 195–201.

Eff, M.N., 2019. A Fundamental Investigation into Intermetallic Formation and Growth in the Aluminum-Iron System Using Resistance-Based Diffusion Couples. Ohio State University.

Eisazadeh, H., Hamedi, M., Halvaee, A., 2010. New parametric study of nugget size in resistance spot welding process using finite element method. Mater. Des. 31, 149–157. https://doi.org/10.1016/j.matdes.2009.06.042.

Han, Z., Orozco, J., Indacochea, J.E., Chen, C.H., 1989. Resistance spot welding: a heat transfer study. Weld. J. 68, 363–371.

Kim, E.W., Eagar, T.W., 1989. Measurement of transient temperature response during resistance spot welding. Weld. J. 68, 303–312.

Kim, J.W., Murugan, S.P., Yoo, J.H., Ashiri, R., Park, Y.D., 2020. Enhancing nugget size and weldable current range of ultra-high-strength steel using multi-pulse resistance spot welding. Sci. Technol. Weld. Join. 25, 235–242. https://doi.org/10.1080/13621718.2019.1680483.

Lane, C.T., Sorensen, C.D., Hunter, G.B., Gedeon, S.A., Eagar, T.W., 1987. Cinematography of resistance spot welding of galvanized steel sheet. Weld. J. 66, 260–265.

Lövenborn, D., 2016. 3D FE Simulations of Resistance Spot Welding. KTH Royal Institute of Technology.

Lu, Y., Peer, A., Abke, T., Kimchi, M., Zhang, W., 2018. Subcritical heat affected zone softening in hot-stamped boron steel during resistance spot welding. Mater. Des. 155, 170–184. https://doi.org/10.1016/j.matdes.2018.05.067.

Mikić, B.B., 1974. Thermal contact conductance; theoretical considerations. Int. J. Heat Mass Transf. 17, 205–214. https://doi.org/10.1016/0017-9310(74)90082-9.

Nied, H.A., 1984. The finite element modeling of the resistance spot welding process. Weld. J. 123–132.

Nielsen, C.V., Zhang, W., Alves, L.M., Bay, N., Martins, P.A.F., 2013. Modeling of Thermo-Electro-Mechanical Manufacturing Processes with Applications in Metal Forming and Resistance Welding. Springer, SpringerBriefs in Applied Sciences and Technology. Springer, London, London. https://doi.org/10.1007/978-1-4471-4643-8.

Nielsen, C.V., Martins, P.A.F., Zhang, W., Bay, N., 2015a. Numerical methods in simulation of resistance welding. Proceedings of the 6th International Conference on Coupled Problems in Science and Engineering 322–333.

Nielsen, C.V., Zhang, W., Perret, W., Martins, P.A.F., Bay, N., 2015b. Three-dimensional simulations of resistance spot welding. Proc. Inst. Mech. Eng. Part D J. Automob. Eng. 229, 885–897. https://doi.org/10.1177/0954407014548740.

Nodeh, I.R., Serajzadeh, S., Kokabi, A.H., 2008. Simulation of welding residual stresses in resistance spot welding, FE modeling and X-ray verification. J. Mater. Process. Technol. 205, 60–69. https://doi.org/10.1016/j.jmatprotec.2007.11.104.

Podržaj, P., Simonĉiĉ, S., 2013. Resistance spot welding control based on the temperature measurement. Sci. Technol. Weld. Join. 18, 551–557. https://doi.org/10.1179/1362171813Y.0000000131.

Saha, D.C., Ji, C.W., Park, Y.D., 2015. Coating behaviour and nugget formation during resistance welding of hot forming steels. Sci. Technol. Weld. Join. 20, 708–720. https://doi.org/10.1179/1362171815Y.0000000054.

Shah, U., Liu, X., 2019. Effects of ultrasonic vibration on resistance spot welding of transformation induced plasticity steel 780 to aluminum alloy AA6061. Mater. Des. 182, 108053 https://doi.org/10.1016/j.matdes.2019.108053.

Wan, X., Wang, Y., Zhang, P., 2014. Modelling the effect of welding current on resistance spot welding of DP600 steel. J. Mater. Process. Technol. 214, 2723–2729. https://doi.org/10.1016/j.jmatprotec.2014.06.009.

Yang, Y.P., Khurana, S., Orth, F., Peterson, W., Babu, S.S., 2006. Development of an integrated computational model to predict the performance of AHSS spot welds: methodology and challenges. Sheet Met. Weld. Conf. XII.